Dual-Action Kinase Inhibitors Control p38α MAP Kinase Threonine Dephosphorylation

Emily J Stadnicki[1,2], Hannes Ludewig[1,3], Ramasamy P Kumar[1,4], Xicong Wang[1], Youwei Qiao[1,5], Dorothee Kern[1,3], and Niels Bradshaw[1,6]

[1]Department of Biochemistry, Brandeis University

[2]Molecular and Cell Biology Program, Brandeis University

[3]Howard Hughes Medical Institute

[4]Present address: Northeastern University

[5]Present address: UMass Medical School

[6]To whom correspondence should be addressed: niels@brandeis.edu

Abstract

Reversible protein phosphorylation directs essential cellular processes including cell-division, cell-growth, cell-death, inflammation, and differentiation. Because of this, small molecule ATP-competitive kinase inhibitors have achieved remarkable clinical success, often achieving target specificity by binding to inactive kinase conformations (type II inhibitors). A key to determining kinase activity, and thus signaling outcome, is the conformational state of kinase activation-loops. Activation-loop phosphorylation is a common regulatory mechanism that promotes kinase activity, while type II inhibitors commonly select inactive activation-loop conformations. We hypothesized that protein phosphatases, which can act as the cell's natural kinase inhibitors, may recognize distinct activation-loop conformations. Using a set of type II inhibitors targeting the MAP kinase p38α, we identified inhibitors that modulate dephosphorylation of the activation-

loop phospho-threonine by WIP1. Our X-ray crystal structures of dual phosphorylated p38α bound to the kinase inhibitors pexmetinib, nilotinib and BIRB796 reveal a shared flipped conformation of the activation-loop with a fully accessible phospho-threonine for WIP1. In contrast, our X-ray structure of apo p38α reveals a very different activation-loop conformation with an inaccessible phospho-threonine, thereby explaining increased rate of dephosphorylation upon inhibitor binding. These findings reveal an unexpected dual-action mechanism for kinase inhibitors combining direct active site kinase inhibition with a global decrease in active phosphorylated kinase species, suggesting a new approach to achieve improved potency and specificity.

Introduction

The MAP kinase p38α is a critical regulatory node for DNA damage response and inflammatory pathways[1–4]. The activation-loop of p38α is dual-phosphorylated (p38α-2p) on a threonine (T180) and tyrosine (Y182). T180 phosphorylation stimulates kinase activity more than 1,000-fold and is sufficient for kinase activity in cells, while Y182 phosphorylation primarily controls autophosphorylation and contributes two- to ten-fold towards activity[5,6]. In the cell, p38α phosphorylation is controlled by upstream kinases, autophosphorylation, and a suite of protein phosphatases[3]. Since p38α activation contributes to inflammatory diseases including myocardial ischemia and neurodegeneration, diverse p38α-specific ATP-competitive inhibitors have been identified and studied in the clinic[7,8]. We hypothesize that stimulation of the physiological mechanism of inactivation–dephosphorylation by protein phosphatases–could be a secondary mechanism of inhibition of effective p38α inhibitors. Such dephosphorylation is executed by

cellular phosphatases including serine/threonine phosphatases WIP1[9–11], PPM1A[12], and PP2A[13] as well as tyrosine phosphatases (PTPs)[14], and dual-specificity phosphatases (DUSPs)[22].

How protein phosphatases target their substrate proteins is a longstanding question[15]. While there are structures of phosphatases bound to peptide substrates[16–19], only a single structure of a phosphatase bound to its full-length substrate protein is known: the plant drought-sensing phosphatase HAB1, which is a metal dependent PPM phosphatase, bound to the unphosphorylated form of its target: the kinase SnRK2.6 (PDB: 3UJG)[20]. Remarkable features of this structure are that the activation-loop of SnRK2.6 is not in an active conformation, and extensive contacts between HAB1 and SnRK2.6 positions the kinase for dephosphorylation. This suggests that orthosteric inhibitors of human kinases could modulate the activity of cognate phosphatases by altering activation-loop conformation. Here we employ enzyme kinetics and X-ray crystallography to show that WIP1 phosphatase activity is indeed stimulated by an inhibitor-mediated flip of activation-loop conformation (Fig. 1A).

Results

Type II p38α MAP kinase inhibitors modulate threonine dephosphorylation by WIP1

First, we measured WIP1 phosphatase activity towards p38α-2p, free, ATP-bound and bound to a panel of type II inhibitors (Fig. 1B and S1D). From an initial panel of thirteen inhibitors, we found that pexmetinib and BIRB796 increased the rate of threonine dephosphorylation (by 10- and 2-fold respectively) (Fig. 1B, S1, and S2). Pexmetinib and BIRB796 share an identical right-side moiety that projects into an allosteric pocket and displaces the activation-loop[21], but differ in their left-sides that bind in the ATP binding site (Fig. 1C). In contrast, SB202190 and LY2228820

decreased the rate of dephosphorylation (by 7-fold) (Fig. 1B) and lack a right-side element (Fig. 1C). In an effort to confirm that the changes in dephosphorylation were caused by inhibitor interaction with p38α, we tested that the inhibitors did not change WIP1 hydrolysis of the generic substrate fluorescein-diphosphate (Fig. S1C). Although the high K_M of WIP1 for p38α-2p prevented us from determining whether the compounds change the k_{cat} or K_M of the reaction, we observed similar effects under single and multiple turnover conditions (Fig. S1A, B). Together, these results demonstrate that type II p38α inhibitors can modulate the rate of WIP1 catalyzed p38α dephosphorylation.

Pexmetinib and BIRB796 present phospho-threonine for dephosphorylation

To determine how WIP1 activity towards p38α is stimulated, we solved X-ray crystal structures of human p38α-2p in unliganded and pexmetinib bound states (Fig. 2A). In the unliganded form, we observe the activation-loop in a similar conformation to murine p38α-2p (PDB: 3PY3), with both phospho-sites inaccessible for WIP1, which catalyzes dephosphorylation via a metal activated water utilized for a planar nucleophilic attack of the phosphate. Therefore, we propose that pT180 must be displaced from this site to be dephosphorylated (Fig. 2A and S3).

In our pexmetinib-bound structure, the allosteric right-side of pexmetinib adopts a binding mode that is incompatible with the activation-loop conformation of the murine and our human apo p38α-2p structures, resulting in a flipped activation-loop. Therefore, pT180 projects outwards and is not resolved in the electron density map, along with its four preceding amino acids (Fig. 2B, 2C and S4A). The new pexmetinib-p38α-2p activation-loop conformation is stabilized by hydrogen bonding of the carbonyl oxygen of pexmetinib to the backbone nitrogen of the catalytic

D168 in the conserved DFG motif, which serves as the hinge at the N-terminal side of the activation-loop (Fig. 2B). Furthermore, the phenyl-ring of F169 stacks against the indazole moiety on the left side of pexmetinib (Fig. 2B) and pY182 is located in a new docking site with the phosphate coordinated by R186, H174 and T175 (Fig. 2A). While the side chain of R186 is flipped to the left to coordinate pY182 in both chains of our human apo p38α-2p structure; in apo p38α-2p from mouse R186 is flipped to the position we detected in our pexmetinib-bound human p38α, and does not coordinate pY182 (only two amino acids are different from human, with H47 being involved in crystal-packing), suggesting flexibility in phospho-tyrosine coordination (Fig. 2A, S3).

Bolstering our conclusion that activation-loop flipping drives dephosphorylation, a similar flip occurs in our structure of p38α-2p bound to BIRB796, which stimulated WIP1 dephosphorylation as well, although to a lesser extent (Fig. 1B and 3A). The DFG motif is anchored by the shared inhibitor right-side (Fig. 1C), and pY182 docks in a similar position as in the pexmetinib bound structure (Fig. 3 and S4). pY182 is solely coordinated by R186 (H174 and T175 are unresolved) in the BIRB796-p38α-2p complex compared to the pexmetinib-p38α-2p complex, suggesting reduced stability of the phospho-tyrosine docking pocket for the former (Fig. 2A, S4 and S5A). We speculate that this difference may result in less favorable presentation of the phospho-threonine to WIP1, contributing to the difference in the measured dephosphorylation rate. Another major difference between the two structures is the αD-helix, which links the N and C-lobes of the kinase structure and sits behind the flipped activation-loop docking site (Fig. 3B). Pexmetinib is present in two conformers (Fig. 2B), one of which has the hydroxyl group on the left side of pexmetinib positioned to make contact with the αD-helix

linker (M109 and A111), which are ordered and resolved. However, BIRB796 lacks these contacts and this region is largely unresolved for BIRB796-p38α-2p (Fig. 3B). These conformational differences offer potential explanations for how chemical differences between these related inhibitors determine stability of the flipped activation-loop conformation and dephosphorylation rate.

A shared conformational state directs p38α dephosphorylation

To determine if any of the hundreds of structures of p38 in the PDB share the flipped activation-loop conformation of pexmetinib and BIRB796 bound p38α-2p, we performed a DALI search[22]. This revealed a structure of human p38α-2p bound to DP802, a compound with similar right-side and shorter left-side compared to pexmetinib and BIRB796 (Fig. S6A, B, PDB: 3NNX, RMSD 0.4 Å to pexmetinib-p38α-2p)[23]. Similar to BIRB796-p38α-2p, H174 and T175 do not coordinate the phosphate of pY182 and the αD-helix is disordered. Although DP802 was not commercially available for phosphatase assays, this structure supports our hypothesis that the shared right side of pexmetinib and BIRB796 is critical for activation-loop flipping and predicts that DP802 would stimulate p38α dephosphorylation to some extent.

A search of deposited kinase structures using KinCoRe[24] revealed one additional structure with a similar activation-loop conformation: unphosphorylated human p38β bound to the ABL inhibitor nilotinib (Tasigna, PDB:3GP0, p38β shares 73.6% sequence identity to p38α). Although nilotinib is not from the same scaffold series as pexmetinib, BIRB796, and DP802, it shares the carbonyl oxygen that coordinates the backbone of D168 (Fig. 1C). In a structure of nilotinib-p38α-2p that we solved, as well as the published structure of nilotinib bound to p38β, DFG and the activation-

loop tyrosine are in a remarkably similar position to our other activation-loop flipped structures (Fig. 3A, B and S6C). However, we note that in nilotinib-p38α-2p, the phosphate-group of pY182 is coordinated by A184 and T185 (Fig. S4B). Consistent with our prediction that the pexmetinib-induced activation-loop conformation presents the phospho-threonine for dephosphorylation, nilotinib stimulated WIP1 dephosphorylation of p38α five-fold (Fig. 1B). In addition, we note that the magnitude of WIP1 stimulating effects correlates inversely with the degree of αD-helix and linker disorder observed in our crystal structures. While pexmetinib-p38α-2p possesses a fully resolved αD-helix and showed the largest potency in stimulating WIP1, BIRB796 lacks a resolved αD-helix when crystallized in complex with p38α-2p and exhibits the lowest stimulating effect (Fig. 3B).

Phospho-tyrosine is not required to stimulate threonine dephosphorylation

While pY182 is in a similar position in all of our activation-loop flipped p38α structures, the coordination of the phosphate is variable, with the most defined coordination occurring for pexmetinib-p38α-2p (Fig. 2A and S5A, B). This raises the question of whether tyrosine phosphorylation is required for activation-loop flipping and phosphatase stimulation. Notably, the flipped activation-loop conformation was even preserved in the structure of nilotinib bound to unphosphorylated p38β (Fig. S6C, PDB: 3GP0). We therefore tested whether tyrosine-phosphorylation is required to stimulate WIP1 dephosphorylation using singly-threonine phosphorylated p38α (with tyrosine 182 substituted with phenylalanine, p38α^{Y182F}-p) (Fig. 4A). p38α^{Y182F}-p dephosphorylation was 2-fold slower than p38α-2p. Notably, the stimulatory effect of pexmetinib was reduced, such that it was similar to BIRB796 and nilotinib (Fig. 4A). This result is consistent with additional contacts from tyrosine phosphorylation stabilizing the

activation-loop flipped conformation of p38α when bound to pexmetinib, and that such stabilization could lead to increased dephosphorylation rates.

Further demonstrating that tyrosine phosphorylation stabilizes activation-loop flipping by pexmetinib, an X-ray crystal structure of unphosphorylated pexmetinib-p38α revealed that the unphosphorylated activation-loop is flipped, with Y182 similarly positioned as pY182 (Fig. 4B). Y182 is not as well coordinated as in the p38α-2p structure, but is anchored from the N-terminal side of the activation-loop by hydrogen bond of D176 to the hydroxyl of Y182. The resolution of the pexmetinib-p38α-unphosphorylated structure is significantly lower than pexmetinig-p38α-2p, also indicative of increased conformational flexibility. Together, we conclude that tyrosine phosphorylation promotes, but is not required for pexmetinib induced presentation of the p38α phospho-threonine for dephosphorylation by WIP1.

Conformationally selective activation-loop recognition is shared across phosphatase families

Since the conformational change of the activation-loop that stimulates WIP1 dephosphorylation exposes pT180, we reasoned that other phosphatases, which would share a requirement for pT180 accessibility (Fig. S3D-H) might similarly be stimulated by the WIP1 stimulating compounds. We surveyed the subset of inhibitors that had the largest effects with three additional phosphatases: PPM1A, a PPM phosphatase related to WIP1 that natively targets p38α[12], DUSP3, a dual specificity (Tyr, Ser/Thr) family phosphatase (related to tyrosine phosphatases) that is capable of dephosphorylating p38α and has been well characterized biochemically[19], as well as alkaline phosphatase from shrimp (SAP). The same trends of dephosphorylation stimulation and

inhibition were observed by inhibitor binding to p38α-2p for these phosphatases, but not to the same as extent as seen for WIP1 (Fig. 5A and S7A, B, C). SAP had the largest change in activity upon inhibitor binding, followed by PPM1A and DUSP3. To determine if this effect was threonine phosphorylation specific, we assayed DUSP3 dephosphorylation of single tyrosine phosphorylated p38α^{T180A}-p in the presence of our five modulating compounds. While the compounds induce small changes in dephosphorylation, the direction and magnitude of effects were distinct from pT180 dephosphorylation in context of both p38α-2p and p38α^{Y182F}-p (Fig. 5B and S7D). Intriguingly, inhibitors that trap the activation-loop of the MAP kinase ERK2 in an inactive conformation (distinct from the flipped-p38α conformation we observe) stimulate ERK tyrosine dephosphorylation[25]. Thus, the modulatory effects of type II inhibitors on p38α dephosphorylation are generalizable across phosphatase families, but the magnitude of change is specific to particular phosphatase/kinase pairs.

Discussion

How can active, p38α-2p be turned off by cognate phosphatases in the cell, given that the phosphorylated residues of the activation-loop are inaccessible for nucleophilic attack as observed in X-ray crystal structures (Fig. S2A-C)? Our new structures of p38α-2p bound to phosphatase stimulating inhibitors delivered an answer to this puzzle; that these inhibitors shift a pre-existing equilibrium of the activation-loop towards a higher population of a dephosphorylation-competent state (Fig. 5C). Our biochemical data suggest that this state exposes the pT180 for dephosphorylation in an activation-loop flipped conformation (Fig. 2A). While there are no structures yet of p38α bound to a cognate phosphatase, there exists a structure of unphosphorylated SnRK2.6 kinase bound to its cognate phosphatase, HAB1 (PDB: 3UJG, a

PPM phosphatase related to WIP1)[20]. In this complex the kinase activation-loop is oriented related to the flipped activation-loop of our liganded-p38α-2p structures, providing a template of how activation-loop flipping could position the target residue for a docked phosphatase (Fig. 5C, S8).

Suggestively, a recent cryo-EM structure of the upstream kinase ($MKK6^{DD}$) trapped in complex with the substrate analogue $p38\alpha^{T180V}$ (PDB: 8A8M), similarly showed the $p38\alpha^{T180V}$ activation-loop redirected towards the orientation that we report for p38α-2p bound to phosphatase stimulating compounds[26] (Fig. 5C). Whereas the activation-loops in our human apo p38α-2p structures and the preexisting murine p38α-2p structure are resistant to post-translational modifications, binding of pexmetinib, BIRB796, or nilotinib shifts the equilibrium towards states that are modification-competent. These modification-competent states are similar, yet not identical, to the aforementioned structures of kinases bound to their respective partners. This leads us to postulate that the activation-loop of p38α samples an ensemble of related, but distinct, modification-competent states that determine the extent to which p38α activation-loop is phosphorylated and dephosphorylated (Fig. 5C and S8).

Could simultaneous stimulation of dephosphorylation and direct competition for ATP binding enhance the potency and/or specificity of kinase inhibition? A type II kinase inhibitor such as pexmetinib, nilotinib, or BIRB796 that stimulates dephosphorylation of its target could achieve increased efficacy through durable inactivation even after disassociating, in contexts where signaling induction is temporally limited. In contrast, compounds such as SB202190 and LY2228820 that inhibit dephosphorylation would therefore increase the pool of active kinase that

requires inhibition, reducing their potency. In addition, cell-type variability of phosphatase activity profiles raises the possibility that specificity conferred by such dual-action inhibition mechanism could enable rationally guided identification of cell-type specific kinase inhibitors.

Our finding that nilotinib stimulates p38α dephosphorylation may provide an example of how phosphatase interaction with type II inhibitors has clinical relevance. Initial biochemical kinase screening identified p38α as a weaker off-target binder of nilotinib (K_d: 460 nM) compared to its primary target ABL (K_d: 10 nM)[27]. However, nilotinib's side effects correlated with p38 inhibition[28] which could be exacerbated by its phosphatase interaction. Conversely, nilotinib has been investigated as a treatment for neurodegenerative diseases including Lewy Body Dementias[29], Alzheimer's disease[30,31], and Parkinson's disease[32], with therapeutic benefit attributed to reduction of inflammation in the brain that could be attributed to p38 inhibition[33]. Similarly, the p38α inhibitor VX-745 (neflamapimod) has shown promise in trials for neurodegenerative diseases with challenges of identifying optimal dosing[29,34]. Thus, our discovery that type II kinase inhibitors can control phosphatase activity towards their targets could enable the development of therapeutics with improved efficacy and emphasizes the importance of determining how kinase conformations control their dephosphorylation.

Methods

Protein expression constructs

Full length PPM1A, p38α, and DUSP3 were generated by isolation of their respective coding sequences from HEK 293 genomic DNA and inserted into pET47b vectors with an N-terminal 6-His tag. Mutations were introduced to the p38 expression construct using the QuikChange site-directed mutagenesis kit (Agilent). pCDFDuet-MKK6-EE was a gift from Kevin Janes (Addgene plasmid # 82718 ; http://n2t.net/addgene:82718 ; RRID:Addgene_82718). The cloning sequence was inserted into a pET47b vector with an N-terminal 6-His tag. The 1-420 WIP1 construct was codon optimized by GenScript and was inserted into a pET28b vector with an N-terminal 6-His SUMO tag.

Protein expression and purification

All proteins were expressed in *E. coli* BL21 (DE3) cells were grown at 37 ºC in Lennox lysogeny broth (LB) to an OD600 of 0.6 and induced at 16 ºC for 14-18 hours with 1 mM isopropyl β-d-1-thiogalactopyranoside (IPTG) unless otherwise specified. Cells were harvested and purified as follows:

WIP1

In addition to 1 mM IPTG cells were induced with 2 mM $MgCl_2$. Cell pellets were resuspended in lysis buffer (50 mM Tris-HCl pH 7.4, 500 mM NaCl, 10 mM $MgCl_2$, 10% (v/v) glycerol, 1 mM dithiothreitol (DTT)) with 1 mM phenylmethylsulphonyl fluoride (PMSF), 1:1000 10 mg/mL (by volume) lysozyme and 1:1000 (by volume) benzonase and were lysed using three

passes in a microfluidizer at 10,000 PSI. Cell lysates were cleared by spinning at 16,000 PRM for 45 minutes in an Avanti JA-20 rotor. 10 mM imidazole was added to the cleared lysates. A HisTrap HP column on an AKTA FPLC was equilibrated with lysis buffer and 6% elution buffer (50 mM Tris-HCl pH 7.4, 500 mM NaCl, 10 mM $MgCl_2$, 10% (v/v) glycerol, 1 mM DTT, 400 mM imidazole). Cleared lysates were then run over a HisTrap HP, washed with 6% elution buffer for 10 column volumes, and eluted over a gradient to 100% elution buffer over 20 column volumes. Purity of fractions was analyzed via SDS-PAGE using a 10% Tris-Tricine polyacrylamide gel stained with Coomassie brilliant blue solution. Protein containing fractions were pooled and the SUMO-His tags were cleaved with 10 µg for every mg total protein of ULP1-R3 protease[35] in dialysis to lysis buffer overnight at 4 ^{o}C. WIP1 was further purified on a Superdex S200 16/600 column equilibrated with lysis buffer. Fractions were pooled, concentrated to 200 µM and treated with a 5-fold molar excess of EDTA to remove metal. Chelated WIP1 was buffer exchanged into storage buffer (50 mM Tris-HCl pH 7.4, 500 mM NaCl, 10% glycerol (v/v)), flash-frozen and stored at -80 ^{o}C.

PPM1A, p38α and p38α mutants

Cell pellets were resuspended in lysis buffer (50 mM HEPES pH 7.5, 200 mM NaCl, 20 mM imidazole, 10% (v/v) glycerol, 0.5 mM DTT) with 1 mM PMSF and were lysed using three passes in a microfluidizer at 10,000 PSI. Cell lysates were cleared by spinning at 16,000 RPM for 45 minutes in an Avanti JA-20 rotor. A HisTrap HP column on an AKTA FPLC was equilibrated with lysis buffer. Cleared lysates were then run over a HisTrap HP, washed with lysis buffer buffer for 10 column volumes, and eluted over a gradient to 100% elution buffer elution buffer (50 mM HEPES pH 7.5, 200 mM NaCl, 400 mM imidazole, 10% (v/v) glycerol,

0.5 mM DTT)) over 20 column volumes. Purity of fractions was analyzed via SDS-PAGE using a 10% Tris-Tricine polyacrylamide gel stained with Coomassie brilliant blue solution. Protein containing fractions were pooled and the 6-His tags were cleaved with 3C protease at a 1:100 protease to protein molar ratio in dialysis to lysis buffer overnight at 4 ºC. Cleaved tags were subtracted by passing over a column containing equilibrated Ni-NTA resin. Proteins were further purified on a Superdex S200 16/600 column equilibrated with lysis buffer. Fractions were pooled, concentrated to 500 µM, flash-frozen and stored at -80ºC.

DUSP3

Cell pellets were resuspended in lysis buffer (50 mM HEPES pH 7.5, 200mM NaCl, 20 mM imidazole, 10% (v/v) glycerol, 0.5 mM DTT) with 1 mM PMSF and were lysed using three passes in a microfluidizer at 10,000 PSI. Cell lysates were cleared by spinning at 16,000 PRM for 45 minutes in an Avanti JA-20 rotor. A HisTrap HP column on an AKTA FPLC was equilibrated with lysis buffer. Cleared lysates were then run over a HisTrap HP, washed with lysis buffer for 10 column volumes, and eluted over a gradient to 100% elution buffer elution buffer (50 mM HEPES pH 7.5, 200 mM NaCl, 400 mM imidazole, 10% (v/v) glycerol, 0.5 mM DTT) over 20 column volumes. Fractions containing protein were pooled, concentrated to 800 µM, flash-frozen and stored at -80ºC.

$MKK6^{EE}$

Cell pellets were resuspended in lysis buffer (50 mM HEPES pH 7.5, 200 mM NaCl, 20 mM imidazole, 10% (v/v) glycerol, 0.5 mM DTT) with 1 mM PMSF and were lysed using three passes in a microfluidizer at 10,000 PSI. Cell lysates were cleared by spinning at 16,000 PRM

for 45 minutes in an Avanti JA-20 rotor. A HisTrap HP column on an AKTA FPLC was equilibrated with lysis buffer. Cleared lysates were then run over a HisTrap HP, washed with lysis buffer for 10 column volumes, and eluted over a gradient to 100% elution buffer elution buffer (50 mM HEPES pH 7.5, 200 mM NaCl, 400 mM imidazole, 10% (v/v) glycerol, 0.5 mM DTT) over 20 column volumes. Purity of fractions was analyzed via SDS-PAGE using a 10% Tris-Tricine polyacrylamide gel stained with Coomassie brilliant blue solution. Protein containing fractions were pooled and were further purified on a Superdex200 16/600 column equilibrated with lysis buffer. Fractions were pooled, concentrated to 500 μM, flash-frozen and stored at -80ºC.

Small molecule reagents

Compound	**Source**	**Cat. #**
pexmetinib	APExBIO (Houston, TX)	B6012
nilotinib	APExBIO (Houston, TX)	A8232
BIRB796	APExBIO (Houston, TX)	A5639
imatinib	APExBIO (Houston, TX)	A3487
SD169	APExBIO (Houston, TX)	C5850
VX-702	APExBIO (Houston, TX)	A8687
FGA-19	Fisher Scientific (Hampton, NH)	5304860001
SB203580	APExBIO (Houston, TX)	A8254
RWJ67657	APExBIO (Houston, TX)	C5316
VX-745	APExBIO (Houston, TX)	A8686
TAK-715	APExBIO (Houston, TX)	A8688

losmapimod	APExBIO (Houston, TX)	B4620
SB202190	APExBIO (Houston, TX)	A1632
LY2228820	APExBIO (Houston, TX)	A5566
Fluorescein diphosphate, tetra ammonium salt (FDP)	Fisher Scientific (Hampton, NH)	501953367

X-ray crystallography

Crystallization

p38α was dual-phosphorylated by $MKK6^{EE}$ using established methods (Kumar et al., 2018). Dual phosphorylation was verified by the protein intact mass measurements using mass spectrometry.

Crystals of p38α-2p apo were obtained by combining 0.3 μL of 8 mg/mL p38α-2p with 0.3 μL of 100 mM BIS-TRIS pH 6.5 and 25% polyethylene glycol (PEG) 3350. Crystals were grown in sitting drops for two weeks at 20 ºC. Crystals were harvested and flash-frozen (liquid N_2) in 15% glycerol.

Crystals of p38α-2p bound to pexmetinib were obtained by combining 0.3 μL of 8 mg/mL p38α-2p + 250 μM pexmetinib for a final DMSO concentration of 5% with 0.3 μL of 100 mM MES pH 6.5, 200 mM ammonium sulfate, 4% propanediol, and 30% PEG8000. Crystals were grown in sitting drops for two weeks at 20 ºC. Crystals were harvested and flash-frozen (liquid N_2) in 15% glycerol.

Crystals of p38α-2p bound to nilotinib were obtained by combining 0.3 μL of 8 mg/mL p38α-2p + 250 μM nilotinib for a final DMSO concentration of 5% in a 0.3 μL reservoir of 100 mM BIS-TRIS pH 6.0 and 23% PEG3350. Crystals were grown in sitting drop for two months at 20 °C. Crystals were harvested and flash-frozen (liquid N_2) in 15% glycerol.

Crystals of p38α-2p bound to BIRB796 were obtained by combining 0.3 μL of 8 mg/mL p38α-2p + 250 μM BIRB796 for a final DMSO concentration of 5% with 0.3 μL reservoir of 100 mM BIS-TRIS pH 5.5, 200 mM ammonium sulfate, and 25% PEG3350. Crystals were grown in sitting drops for two weeks at 20°C. Crystals were harvested and flash-frozen (liquid N_2) in 15% glycerol.

Crystals of p38α bound to pexmetinib were obtained by combining 0.3 μL of 8 mg/mL p38α + 250 μM pexmetinib for a final DMSO concentration of 5% in a 0.3 μL reservoir of 100 mM MES pH 6.0, 200 mM ammonium sulfate, 4% propanediol, and 20% PEG6000. Crystals were grown in sitting drops for two weeks at 20 °C. Crystals were harvested and flash-frozen (liquid N_2) in 15% glycerol.

Data collection and processing

Cryogenic (100 K) X-ray diffraction data of single crystals were collected at Advanced Light Source (Lawrence Berkeley National Laboratory) at beamlines 2.0.1 (p38α-2p and pexmetinib-p38α-2p) and 8.2.2 (nilotinib-p38α-2p, BIRB796-p38α-2p and pexmetinib-p38α). The data were integrated with XDS[36], scaled and merged in Aimless[37], and data quality was assessed using

Xtriage (Phenix)[38]. Structures of p38α-2p and pexmetinib-p38α-2p were solved by molecular replacement using Phaser (Phenix)[39] utilizing as a search model chain A of 3PY3 (murine p38α-2p). Initial phases for nilotinib-p38α-2p, BIRB796-p38α-2p and pexmetinib-p38α were obtained using pexmetinib-p38α-2p as a search model.

Refinement and model building

Refinement and manual model building were performed using phenix.refine (Version 1.20.1)[40] and Coot,[41] respectively. Models were validated using MolProbity[42]. Figures of structure models were created using ChimeraX[43].

Phosphatase assays

All phosphatase assays were performed with p38α-2p that was labeled with ^{32}P by incubating p38α (25 μM), 6His-MKK6^{EE} (0.625 μM), and 20 μCi of γ-^{32}P ATP for 6-8 hours at room temperature in 20 mM HEPES pH 7.5, 0.5 mM EDTA, 20 mM $MgCl_2$, 2 mM DTT. Following initial incubation, excess cold ATP was added for a final concentration of 12 mM and was incubated overnight. This results in dual-phosphorylated p38α with the ^{32}p nearly exclusively incorporated on T180 (Fig. S2). Unincorporated nucleotide was removed by buffer exchange using a Zeba spin column equilibrated in 50 mM HEPES pH 7.5, 100 mM NaCl. 6His-MKK6^{EE} was then removed by Ni-NTA resin equilibrated in 50 mM HEPES pH 7.5, 100 mM NaCl, 20 mM imidazole. The flow-through fraction from the Ni-NTA resin containing p38α-^{32}p was then exchanged into 50 mM HEPES pH 7.5, 100 mM NaCl buffer using 3 subsequent Zeba spin columns to remove all unincorporated nucleotide and free phosphate. Labeled p38α-^{32}p was aliquoted and frozen at -80°C for future use.

WIP1 and PPM1A

All WIP1 phosphatase assays were performed at room temperature in 50 mM HEPES pH 7.5, 0.8 mM CHAPS, 0.05 mg/mL BSA, and 15 mM $MnCl_2$. WIP1 concentration was 2.5 μM, PPM1A concentration was 0.5 μM and p38α-^{32}p was 0.25 μM unless otherwise stated. 1.25 μM p38α inhibitors were added to reactions at a 5% final DMSO concentration immediately before the start of the reaction. Reactions were stopped with 0.5 M EDTA, pH 8.0 and run on PEI-Cellulose TLC plates developed in 1 M $LiCl_2$ and 0.8 M acetic acid and imaged on a Typhoon scanner. Phosphatase assays were performed more than three independent times as separate experiments.

DUSP3

All DUSP3 phosphatase assays were performed in 50 mM HEPES pH 7.5 and 100 mM NaCl. Reactions were stopped with SDS and run on PEI-Cellulose TLC plates run through water then developed in 1 M $LiCl_2$ and 0.8 M acetic acid and imaged on a Typhoon scanner. Phosphatase assays were performed more than three independent times as separate experiments. Data shown in figures is from a single representative experiment, and reported errors are the error from the fit unless indicated otherwise. Reactions with p38α-2p were run at 37 °C with 50 μM DUSP3 and 0.25 μM ^{32}pT180 labeled p38α-2p. 1.25 μM p38α inhibitors were added to reactions at a 5% final DMSO concentration immediately before the start of the reaction. Reactions with ^{32}pY182 labeled p38α^{T180A}-p were run at room temperature with 15 μM DUSP3 and 0.25 μM ^{32}pY182 labeled p38α^{T180A}-p. 1.25 μM p38α inhibitors were added to reactions at a 5% final DMSO concentration immediately before the start of the reaction.

SAP

All SAP phosphatase assays were performed at 37 °C in 1x SAP reaction buffer. SAP concentration was 1 unit per 5 μL reaction and p38α-^{32}p concentration was 0.25 μM. 1.25 μM p38α inhibitors were added to reactions at a 5% final DMSO concentration immediately before the start of the reaction. Reactions were stopped with SDS and run on PEI-Cellulose TLC plates run through water then developed in 1 M $LiCl_2$ and 0.8 M acetic acid and imaged on a Typhoon scanner. Phosphatase assays were performed more than three independent times as separate experiments. Data shown in figures is from a single representative experiment, and reported errors are the error from the fit unless indicated otherwise.

Fluorescein diphosphate phosphatase assay

All FDP reactions were performed at 25 °C in a Corning 3573 384-well black flat bottom plate in 50 mM K HEPES pH 7.5, 0.8 mM CHAPS, 0.05 mg/mL BSA, 10 mM $MnCl_2$, 30 nM WIP1 and 50 μM FDP. 1.25 μM p38α inhibitors were added at a final DMSO concentration of 5% immediately before the start of the reaction. Fluorescence (λ_{ex}: 470 nm λ_{em}: 530 nm) was read on a plate reader taking timepoints every 30 seconds at a constant temperature of 25 ºC.

References

1. Ronkina, N. & Gaestel, M. MAPK-Activated Protein Kinases: Servant or Partner? *Annu. Rev. Biochem.* **91**, 505–540 (2022).

2. Roux, P. P. & Blenis, J. ERK and p38 MAPK-activated protein kinases: a family of protein kinases with diverse biological functions. *Microbiology and Molecular Biology Reviews* **68**, 320–344 (2004).

3. ZARUBIN, T. & Han, J. Activation and signaling of the p38 MAP kinase pathway. *Cell Res* **15**, 11–18 (2005).

4. Canovas, B. & Nebreda, A. R. Diversity and versatility of p38 kinase signalling in health and disease. *Nat. Rev. Mol. Cell Biol.* **22**, 346–366 (2021).

5. Askari, N., Beenstock, J., Livnah, O. & Engelberg, D. p38α Is Active in Vitro and in Vivo When Monophosphorylated at Threonine 180. *Biochemistry* **48**, 2497–2504 (2009).

6. Zhang, Y.-Y., Mei, Z.-Q., Wu, J.-W. & Wang, Z.-X. Enzymatic Activity and Substrate Specificity of Mitogen-activated Protein Kinase p38α in Different Phosphorylation States*. *J. Biol. Chem.* **283**, 26591–26601 (2008).

7. Haller, V., Nahidino, P., Forster, M. & Laufer, S. A. An updated patent review of p38 MAP kinase inhibitors (2014-2019). *Expert Opin Ther Pat* **30**, 453–466 (2020).

8. Kompa, A. R. Do p38 mitogen-activated protein kinase inhibitors have a future for the treatment of cardiovascular disease? *J Thorac Dis* **8**, E1068–E1071 (2016).

9. Takekawa, M. *et al.* p53-inducible wip1 phosphatase mediates a negative feedback regulation of p38 MAPK-p53 signaling in response to UV radiation. *EMBO J* **19**, 6517–6526 (2000).

10. Yamaguchi, H. *et al.* Substrate specificity of the human protein phosphatase 2Cdelta, Wip1. *Biochemistry* **44**, 5285–5294 (2005).

11. Gilmartin, A. G. *et al.* Allosteric Wip1 phosphatase inhibition through flap-subdomain interaction. *Nat Chem Biol* **10**, 181–187 (2014).

12. Takekawa, M., Maeda, T. & Saito, H. Protein phosphatase 2Calpha inhibits the human stress-responsive p38 and JNK MAPK pathways. *EMBO J.* **17**, 4744–4752 (1998).

13. Lee, T., Kim, S. J. & Sumpio, B. E. Role of PP2A in the regulation of p38 MAPK activation in bovine aortic endothelial cells exposed to cyclic strain. *J. Cell. Physiol.* **194**, 349–355 (2003).

14. Muñoz, J. J., Tárrega, C., Blanco-Aparicio, C. & Pulido, R. Differential interaction of the tyrosine phosphatases PTP-SL, STEP and HePTP with the mitogen-activated protein kinases ERK1/2 and p38alpha is determined by a kinase specificity sequence and influenced by reducing agents. *Biochem J* **372**, 193–201 (2003).

15. Shi, Y. Serine/threonine phosphatases: mechanism through structure. *Cell* **139**, 468–484 (2009).

16. Salmeen, A., Andersen, J. N., Myers, M. P., Tonks, N. K. & Barford, D. Molecular basis for the dephosphorylation of the activation segment of the insulin receptor by protein tyrosine phosphatase 1B. *Mol Cell* **6**, 1401–1412 (2000).

17. Zeke, A. *et al.* Structural insights into the pSer/pThr dependent regulation of the SHP2 tyrosine phosphatase in insulin and CD28 signaling. *Nat. Commun.* **13**, 5439 (2022).

18. Debnath, S. *et al.* A trapped human PPM1A-phosphopeptide complex reveals structural features critical for regulation of PPM protein phosphatase activity. *J Biol Chem* (2018) doi:10.1074/jbc.ra117.001213.

19. Schumacher, M. A., Todd, J. L., Rice, A. E., Tanner, K. G. & Denu, J. M. Structural basis for the recognition of a bisphosphorylated MAP kinase peptide by human VHR protein Phosphatase. *Biochemistry* **41**, 3009–3017 (2002).

20. Soon, F.-F. *et al.* Molecular mimicry regulates ABA signaling by SnRK2 kinases and PP2C phosphatases. *Science* **335**, 85–88 (2012).

21. Pargellis, C. *et al.* Inhibition of p38 MAP kinase by utilizing a novel allosteric binding site. *Nat. Struct. Biol.* **9**, 268–272 (2002).

22. Holm, L. & Rosenström, P. Dali server: conservation mapping in 3D. *Nucleic Acids Research* **38**, W545-9 (2010).

23. Ahn, Y. M. *et al.* Switch control pocket inhibitors of p38-MAP kinase. Durable type II inhibitors that do not require binding into the canonical ATP hinge region. *Bioorg. Med. Chem. Lett.* **20**, 5793–5798 (2010).

24. Modi, V. & Dunbrack, R. L. Kincore: a web resource for structural classification of protein kinases and their inhibitors. *Nucleic Acids Res.* **50**, D654–D664 (2021).

25. Pegram, L. M. *et al.* Activation loop dynamics are controlled by conformation-selective inhibitors of ERK2. *Proc Natl Acad Sci USA* **116**, 15463–15468 (2019).

26. Juyoux, P. *et al.* Architecture of the MKK6-p38α complex defines the basis of MAPK specificity and activation. *Science* **381**, 1217–1225 (2023).

27. Davis, M. I. *et al.* Comprehensive analysis of kinase inhibitor selectivity. *Nat. Biotechnol.* **29**, 1046–1051 (2011).

28. Contreras, O., Villarreal, M. & Brandan, E. Nilotinib impairs skeletal myogenesis by increasing myoblast proliferation. *Skelet. Muscle* **8**, 5 (2018).

29. Skylar-Scott, I. A. & Sha, S. J. Lewy Body Dementia: An Overview of Promising Therapeutics. *Curr. Neurol. Neurosci. Rep.* **23**, 581–592 (2023).

30. Stevenson, M. *et al.* Inhibition of discoidin domain receptor (DDR)-1 with nilotinib alters CSF miRNAs and is associated with reduced inflammation and vascular fibrosis in Alzheimer's disease. *J. Neuroinflammation* **20**, 116 (2023).

31. Turner, R. S. *et al.* Nilotinib Effects on Safety, Tolerability, and Biomarkers in Alzheimer's Disease. *Ann. Neurol.* **88**, 183–194 (2020).

32. Pagan, Fernando. L. *et al.* Nilotinib Effects on Safety, Tolerability, and Potential Biomarkers in Parkinson Disease. *JAMA Neurol.* **77**, 309–317 (2020).

33. Kim, J., Lee, H., Park, J.-H., Cha, B.-Y. & Hoe, H.-S. Nilotinib modulates LPS-induced cognitive impairment and neuroinflammatory responses by regulating P38/STAT3 signaling. *J. Neuroinflammation* **19**, 187 (2022).

34. Jiang, Y. *et al.* Preclinical and randomized clinical evaluation of the p38α kinase inhibitor neflamapimod for basal forebrain cholinergic degeneration. *Nat Commun* **13**, 5308 (2022).

35. Lau, Y.-T. K. *et al.* Discovery and engineering of enhanced SUMO protease enzymes. *J. Biol. Chem.* **293**, 13224–13233 (2018).

36. Kabsch, W. XDS. *Acta Crystallogr. Sect. D* **66**, 125–132 (2010).

37. Evans, P. R. & Murshudov, G. N. How good are my data and what is the resolution? *Acta Crystallogr. Sect. D: Biol. Crystallogr.* **69**, 1204–1214 (2013).

38. Liebschner, D. *et al.* Macromolecular structure determination using X-rays, neutrons and electrons: recent developments in Phenix. *Acta Crystallogr. Sect. D* **75**, 861–877 (2019).

39. McCoy, A. J. *et al.* Phaser crystallographic software. *J Appl Crystallogr* **40**, 658–674 (2007).

40. Afonine, P. V. *et al.* Towards automated crystallographic structure refinement with phenix.refine. *Acta Crystallogr. Sect. D: Biol. Crystallogr.* **68**, 352–367 (2012).

41. Emsley, P., Lohkamp, B., Scott, W. G. & Cowtan, K. Features and development of Coot. *Acta Crystallogr D Biol Crystallogr* **66**, 486–501 (2010).

42. Williams, C. J. *et al.* MolProbity: More and better reference data for improved all-atom structure validation. *Protein Sci.* **27**, 293–315 (2018).

43. Pettersen, E. F. *et al.* UCSF ChimeraX: Structure visualization for researchers, educators, and developers. *Protein Science* **30**, 70–82 (2021).

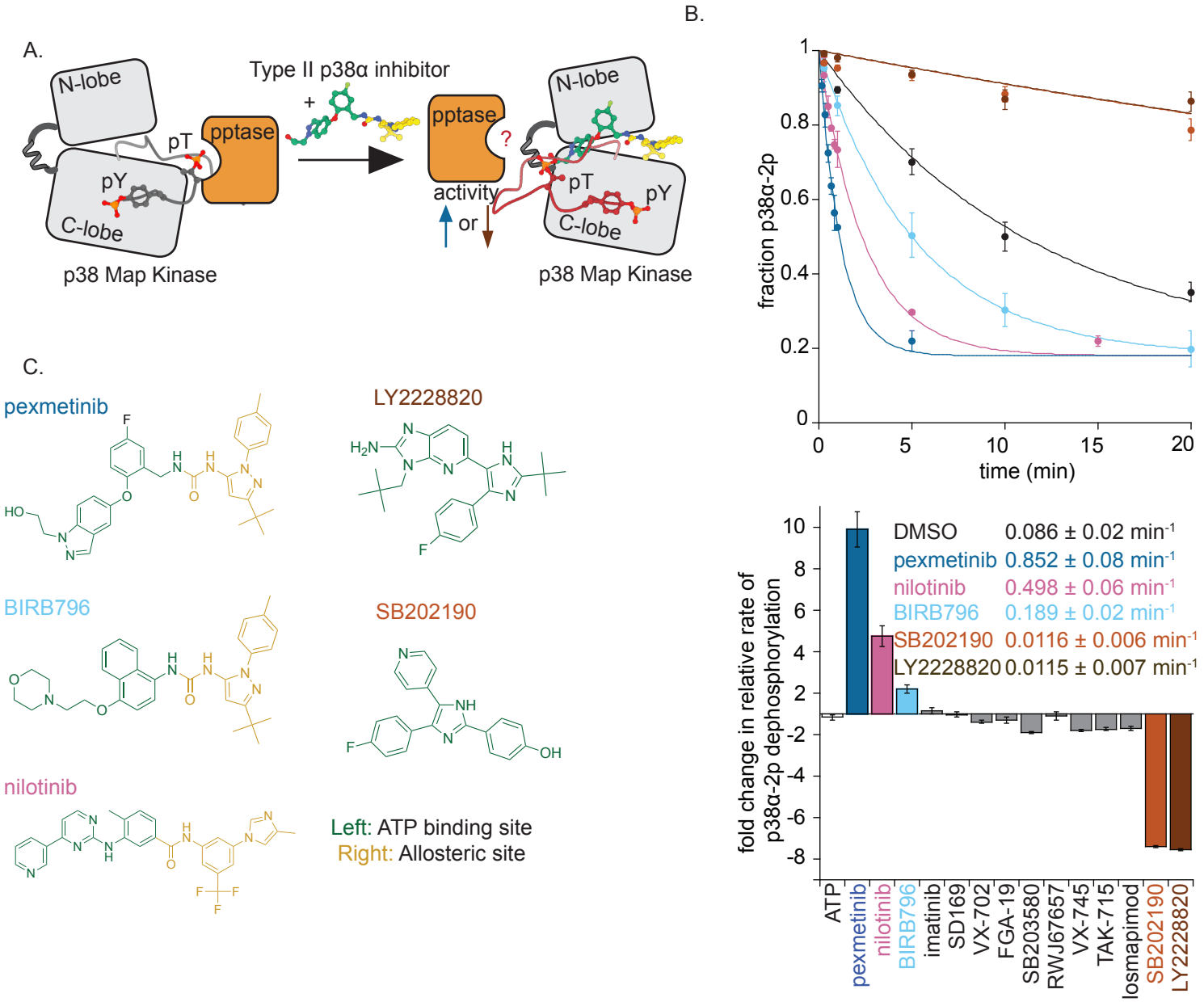

Figure1: Type II p38α inhibitors modulate dephosphorylation of p38α by WIP1 phosphatase. (A) Schematic describing the mechanism of type II p38α inhibitors causing a change in activation-loop conformation. This is followed by a change in phosphatase activity on phosphorylated p38α MAP Kinase. Phosphorylation sites pT180 and pY182 are depicted as spheres and sticks on activation-loop cartoon. (B) Top panel shows single turnover kinetics of p38 α (0.25 μM) dephosphorylation at pT180 by WIP1 (2.5 μM) in the absence or presence of excess p38α inhibitors (1.25 μM). Data are fit to an exponential decay (k_{obs} displayed were averaged from an n=3 ± 1 SD). Bottom panel shows the fold change in k_{obs} in the presence of inhibitors relative to a DMSO treated control (error displayed is the propagated error of the fit). (C) Chemical structures of inhibitors that had the largest impact on phosphatase activity. The ATP binding motif is colored in green and the portion extending into the allosteric pocket is colored in yellow.

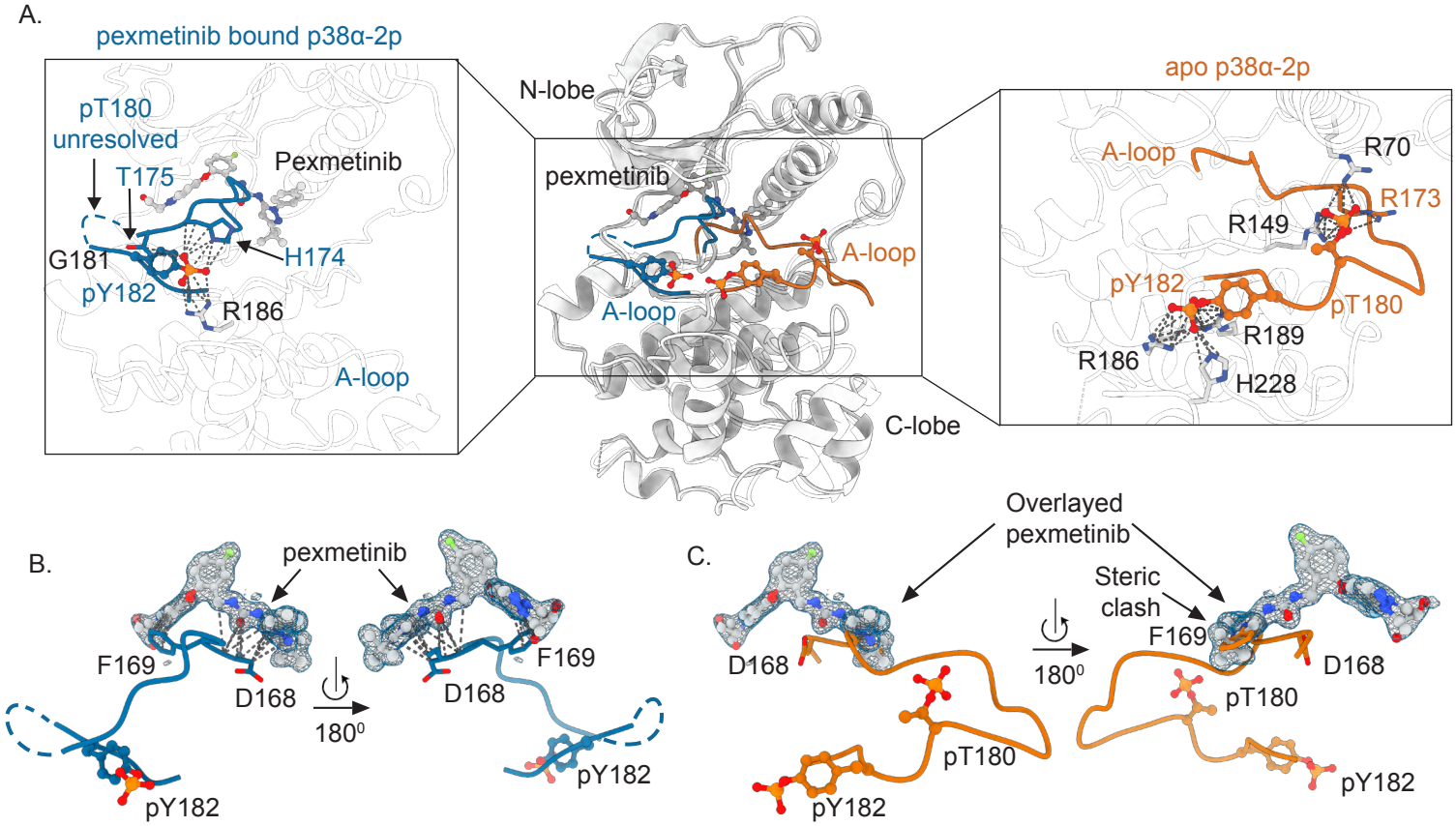

Figure 2: WIP1-stimulating p38α inhibitors induce an activation-loop conformation that exposes pT180 for dephosphorylation. (A) Overlay of X-ray crystal structure of human apo p38 α-2p (A-loop colored orange) and pexmetinib bound human p38α-2p (A-loop in blue) emphasizing activation-loop and phosphorylation site rearrangements. Left zoom shows pexmetinib mediated A-loop conformation and coordination of pY182. Note that pT180 is unresolved, likely due to flexibility. Right zoom shows apo p38α-2p A-loop and coordination of pT180 and pY182. Grey dotted lines indicate any interaction within 4.0 Å of the phosphate group. (B) Activation-loop of p38 α-2p bound pexmetinib (blue) with D168 and F169 shown as sticks and pY182 shown as spheres and sticks. 2Fo-Fc electron density of pexmetinib (contoured at 1 σ within 1.5 Å) is displayed as a mesh. Grey dotted lines indicate any interaction within 4.0 Å of pexmetinib to D168 and F169 (DFG motif). Left panel is rotated 180° and shown in the right panel as indicated by the arrow. (C) Activation-loop of p38α-2p (orange) overlayed with pexmetinib (2Fo-Fc electron density contoured at 1 σ within 1.5 Å) to emphasize the clash of pexmetinib with D168. D168 and F169 are shown in sticks whereas pY182 is shown as spheres and sticks. Left panel is rotated 180° and shown in the right panel as indicated by the arrow. In all structures, oxygen, nitrogen, phosphorous and fluorine atoms are colored red, blue, orange and light green, respectively.

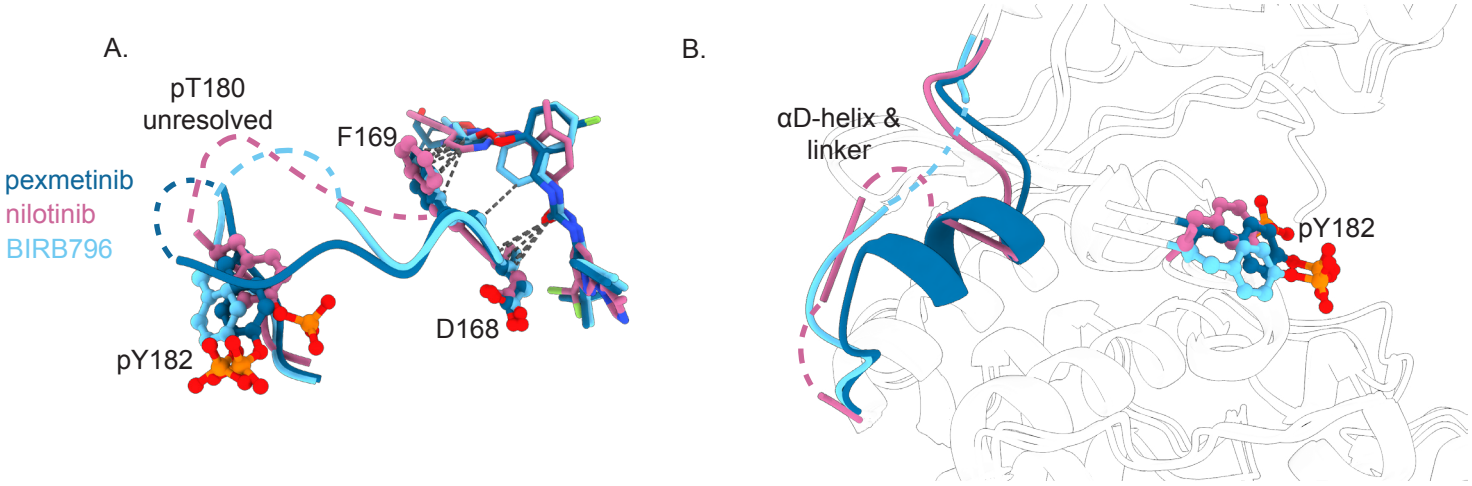

Figure 3: Common activation-loop flip is observed also with BIRB796 and nilotinib. (A) Overlay of the activation-loops of X-ray crystal structures of human p38α-2p bound to pexmetinib (dark blue), human p38α-2p bound to nilotinib (pink), and BIRB796 bound to human p38α-2p (light blue). D168 and F169 are shown in sticks whereas pY182 is shown as spheres and sticks. pT180 is unresolved and exposed in all 3 structures. (B) Overlay of the 3 ligand bound X-ray crystal structures, emphasizing the N- and C- lobe linker and αD-helix (109-123) shown in various colors: human p38α-2p bound to pexmetinib (dark blue), human p38α-2p bound to nilotinib (pink), and BIRB796 bound human p38α-2p (light blue). pY182 is shown as spheres and sticks in the respective colors. The degree of order in the linker region and αD-helix strongly correlates with the magnitude of WIP1 stimulation of p38α-2p dephosphorylation. In all structures, oxygen, nitrogen, phosphorous and fluorine atoms are colored red, blue, orange and light green, respectively.

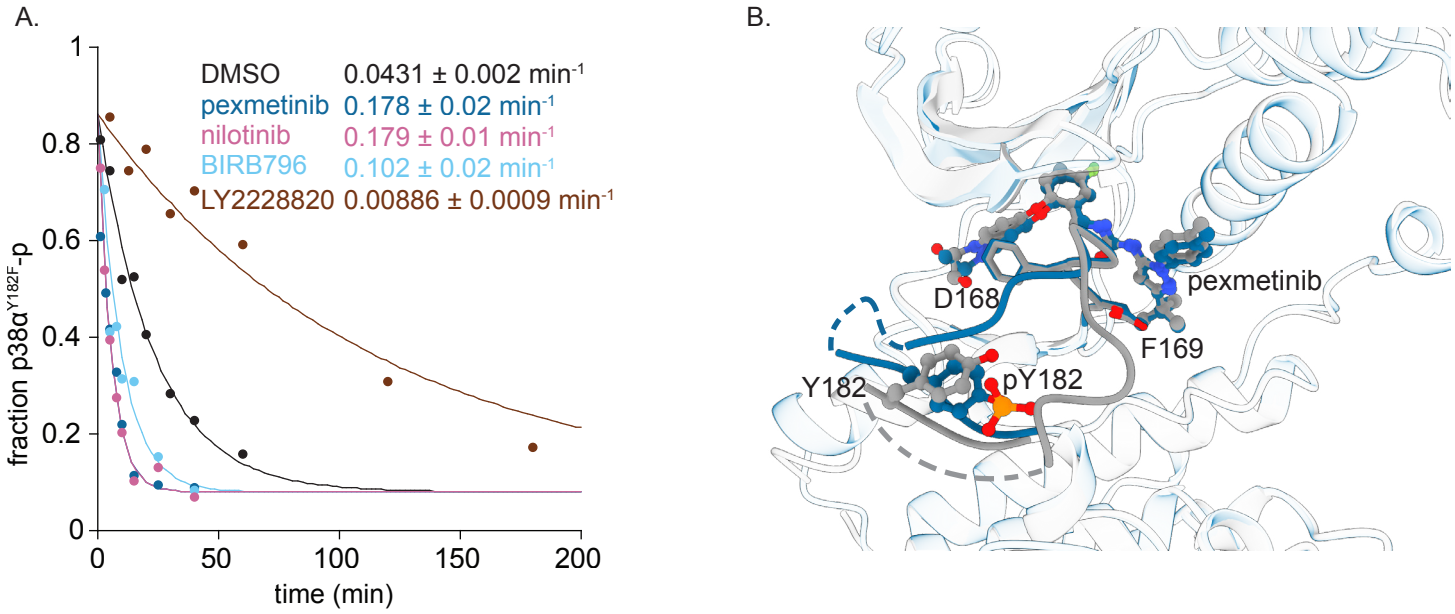

Figure 4: Tyrosine phosphorylation is not required for stimulation of WIP1. (A) Single turnover kinetics (WIP1: 2.5 μM) of single threonine phosphorylated p38α^{Y182F}-p (0.25 μM) in the absence or presence of excess p38α inhibitors (1.25 μM). Data were fit to an exponential decay (n=2 ± error of the fit). (B) X-ray crystal structure of unphosphorylated p38α bound to pexmetinib (grey) overlayed with p38α-2p bound to pexmetinib, showing a similar activation-loop conformation. D168 and F169 are shown in sticks whereas pY182 (pexmetinib-p38α-2p) and Y182 (pexmetinib-p38α) are shown as spheres and sticks. In all structures, oxygen, nitrogen, phosphorous and fluorine atoms are colored red, blue, orange and light green, respectively

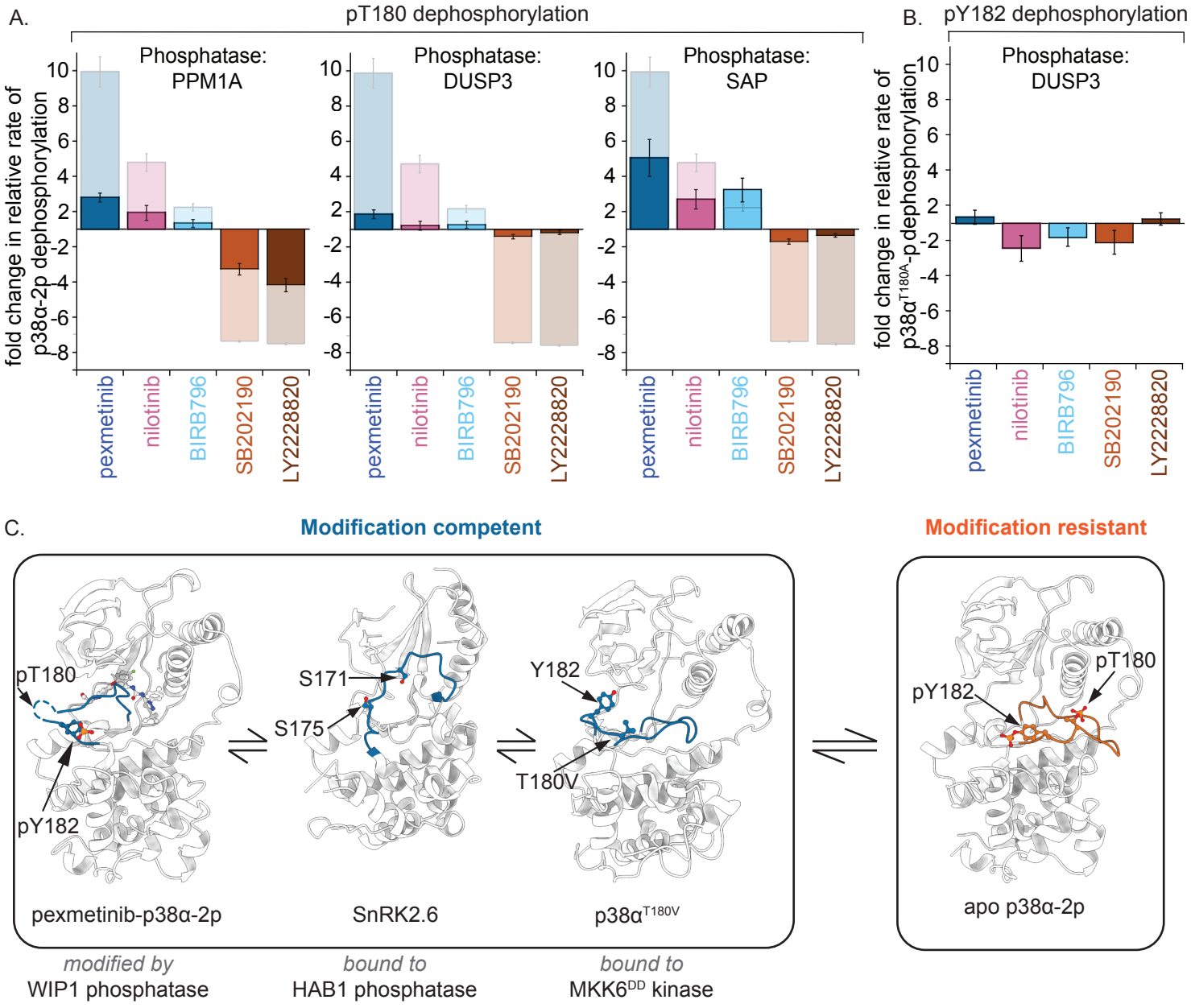

Figure 5: p38α exists in a conformational equilibrium that facilitates dephosphorylation between multiple phosphatases. (A) Fold change comparisons of p38α (0.25 μM) dephosphorylation rates by SAP (1 μM), PPM1A (0.5 μM), and DUSP3 (50 μM) which are all unique phosphatases that can target p38α, in the presence of excess inhibitor (1.25 μM) (error displayed is the propagated error of the fit). Fold change of rates for WIP1 (Fig 1B) are shown as translucent background bars on each plot as a reference. (B) Fold change comparison rate of dephosphorylation of pY182 of p38α^{T180A} (0.25 μM) by DUSP3 (15 μM) in the presence of excess inhibitor (1.25 μM). Error displayed is the propagated error of the fit (n=2). (C) Model proposing a conformational equilibrium between modification resistant (human apo p38α-2p) with inaccessible phosphorylation states and modification competent (pexmetinib-p38α-2p, HAB1-SnRK2.6, and MKK6^{DD}-p38α^{T180V} shown respectively) states that exhibit exposed phosphorylation sites.

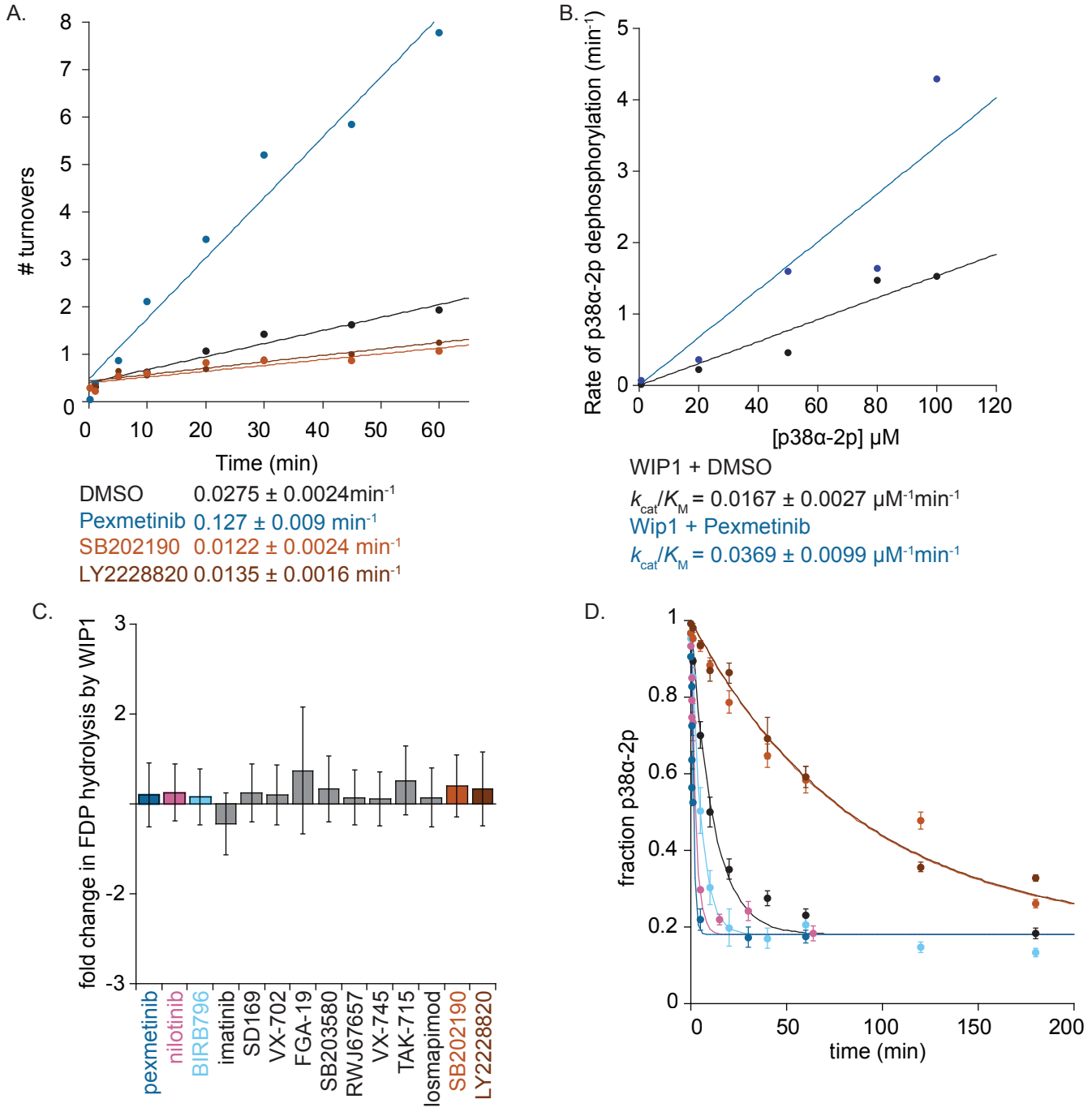

Figure S1: Multiple turnover conditions do not affect the indirect effect of compounds on Wip1 catalyzed p38α dephosphorylation. (A) Multiple turnover reactions of WIP1 (0.25 μM) dephosphorylation of p38α-2p (20 μM) showing similar inhibitor effect compared to single turnover reactions (Fig. 1B). Rates are determined from a linear regression (n=2 ± error of the fit) (B) Multiple turnover WIP1 (0.25 μM) concentration dependence of p38α-2p (concentrations shown on x-axis) in the absence or presence of excess (2-fold molar excess) of pexmetinib. Specificity constant k_{cat}/K_M were determined from a linear regression (n=2 ± error of the fit). (C) Multiple turnover kinetics of fluorescein diphosphate (FDP) (50 μM) hydrolysis by WIP1 (30 nM) in the absence and presence of 1.25 μM inhibitors showing no change in WIP1 activity toward a generic substrate with the addition of p38α inhibitors. Data is shown as the fold change in k_{obs} in the presence of inhibitors relative to a DMSO treated control (error displayed is the propagated error of the fit). (D) Single turnover kinetics of dephosphorylation of p38α (0.25 μM) pT180 by WIP1 (2.5 μM) in the absence or presence of excess p38 inhibitors (1.25 μM). Data are fit to an exponential decay (k_{obs} are displayed were averaged from an n=3 ± 1 SD). Expanded plot from Fig 1B.

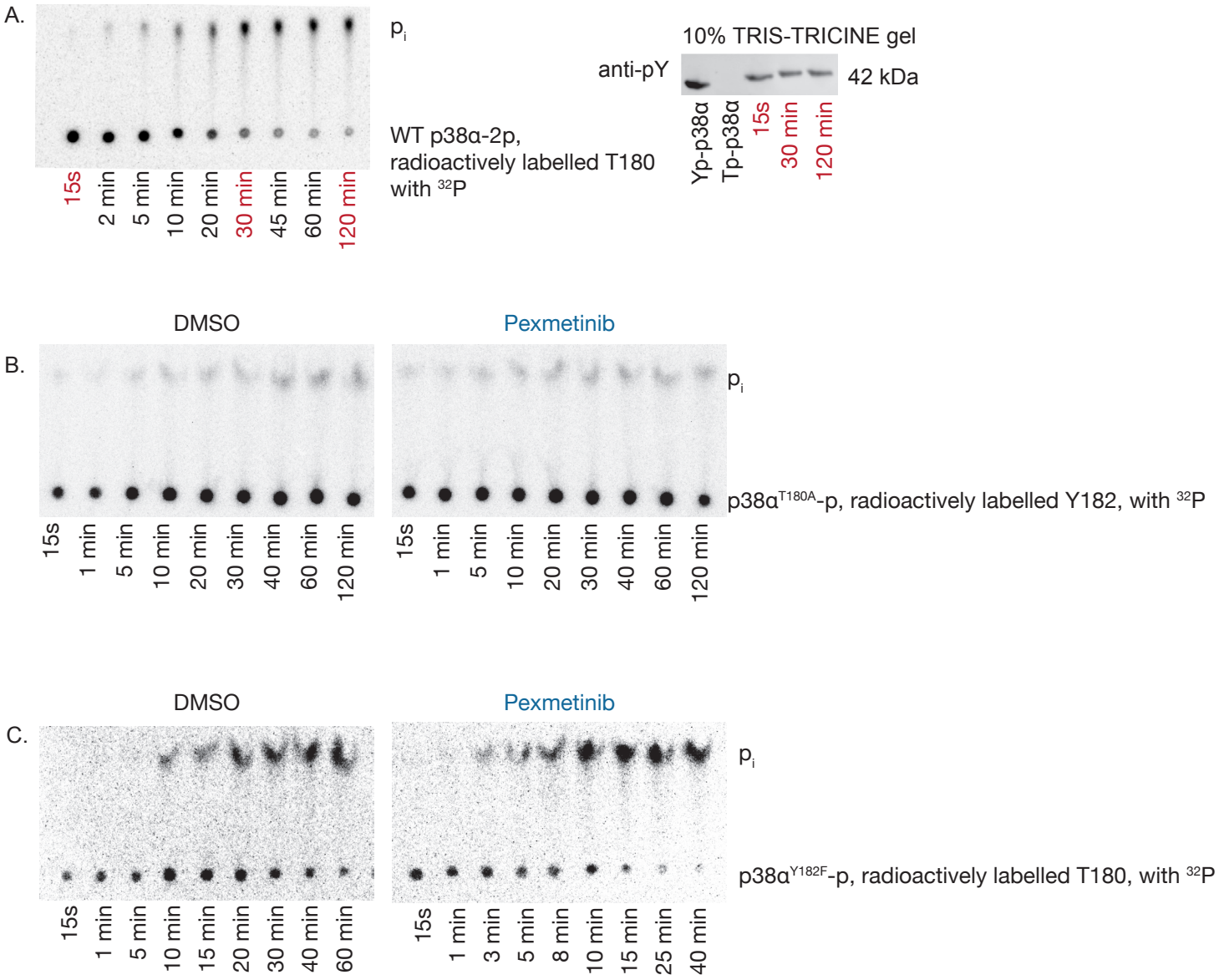

Figure S2: MKK6EE preferentially phosphorylates T180 and WIP1 dephosphorylates only pT180. (A) Dephosphorylation of p38α-2p (0.25 μM) by WIP1 (2.5 μM) over time. Reaction is visualized on a TLC plate over time. p38α-2p (radioactively labelled T180, with ^{32}P) substrate is seen on the bottom and radioactive free phosphate is the product at the top of the TLC plate (left panel). Time points in red are shown on a western blot on the right, probed for phospho-tyrosine, showing no pY dephosphorylation over the reaction time course. This indicates that the sequential addition of sub saturating γ-^{32}P ATP followed by excess cold ATP during the phosphorylation reaction by MKK6^{EE} results in a sample of p38α-2p which is radioactively labeled exclusively on pT180. Therefore, the measured rates of p38α-2p dephosphorylation are p38α-2p (radioactive T180, with ^{32}P) in the context of p38α-2p. (B) Dephosphorylation of p38α^{T180A}-p (0.25 μM, radioactive Y182, with ^{32}P) by WIP1 (2.5 μM) in the absence (left) or presence (right) of excess pexmetinib (1.25 μM) shown on a TLC plate over time. p38α^{T180A}-p (with ^{32}P) substrate is seen on the bottom and radioactive free phosphate is the product at the top of the TLC plate. WIP1 cannot dephosphorylate p38α^{Y182F}-p (with ^{32}P). (C) Dephosphorylation of p38α^{Y182F}-p (0.25 μM with ^{32}P) by WIP1 (2.5 μM) in the absence (left) or presence (right) of excess pexmetinib (1.25 μM) shown on a TLC plate over time. p38α^{Y182F}-p (with ^{32}P) is seen on the bottom and radioactive free phosphate is the product at the top of the TLC plate.

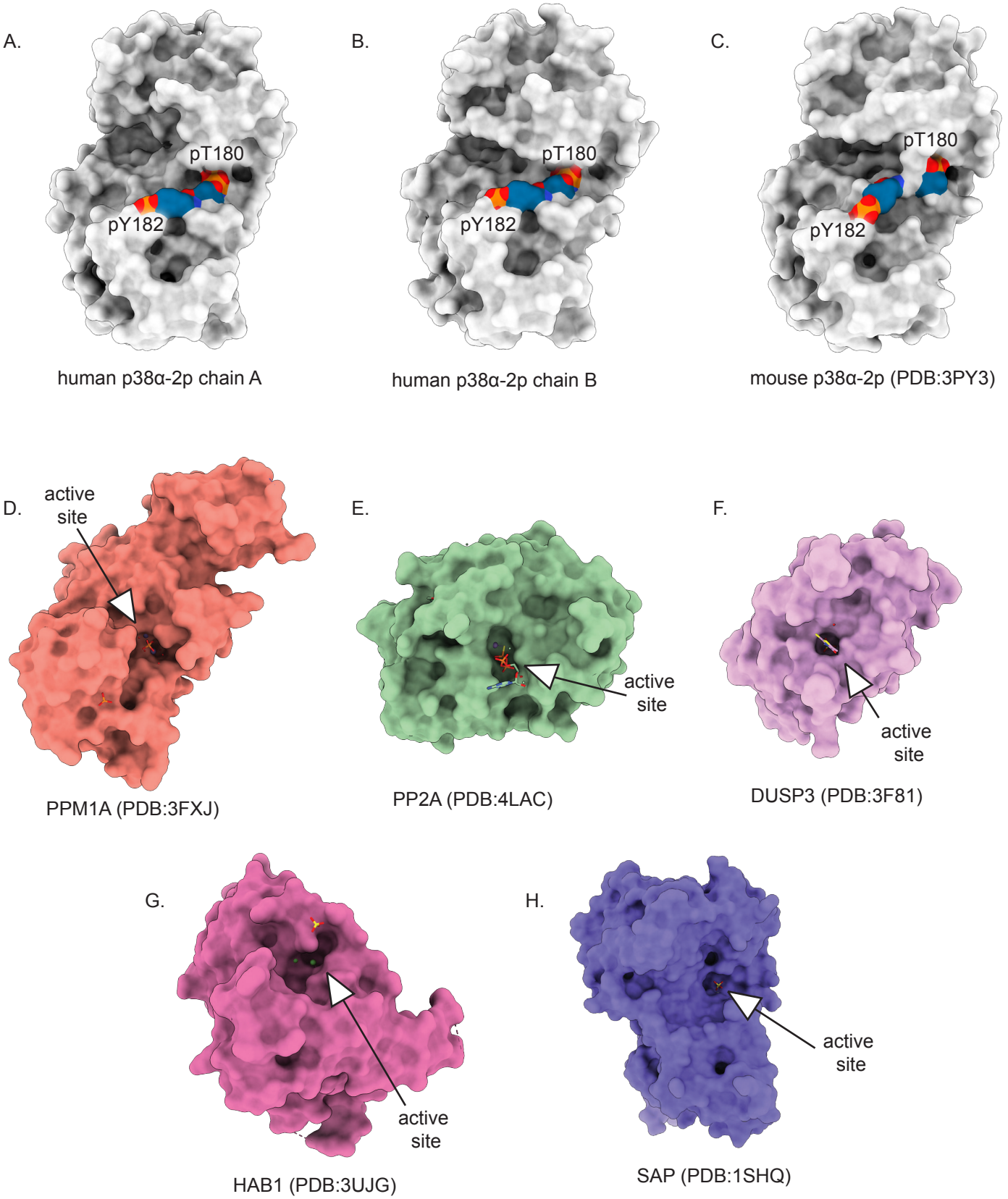

Figure S3: p38α-2p phosphorylation sites are inaccessible to phosphatases. (A-C) Surface representation of human p38α-2p chain A (A) and chain B (B) and murine p38α-2p (C) showing the phosphorylation sites (pT180 and pY182) are inaccessible by phosphatases. (D-H) Surface representation of various families of phosphatases that target kinases with a white arrow indicating their active site. The active sites are occupied by the following (D) phosphate ion, (E) ATPγS, (F) small molecule inhibitor SA3, (G) magnesium (green sphere) and sulfate ion (yellow sphere), and (H) a sulfate ion. In all structures, oxygen, nitrogen, phosphorous and fluorine atoms are colored red, blue, orange and light green, respectively.

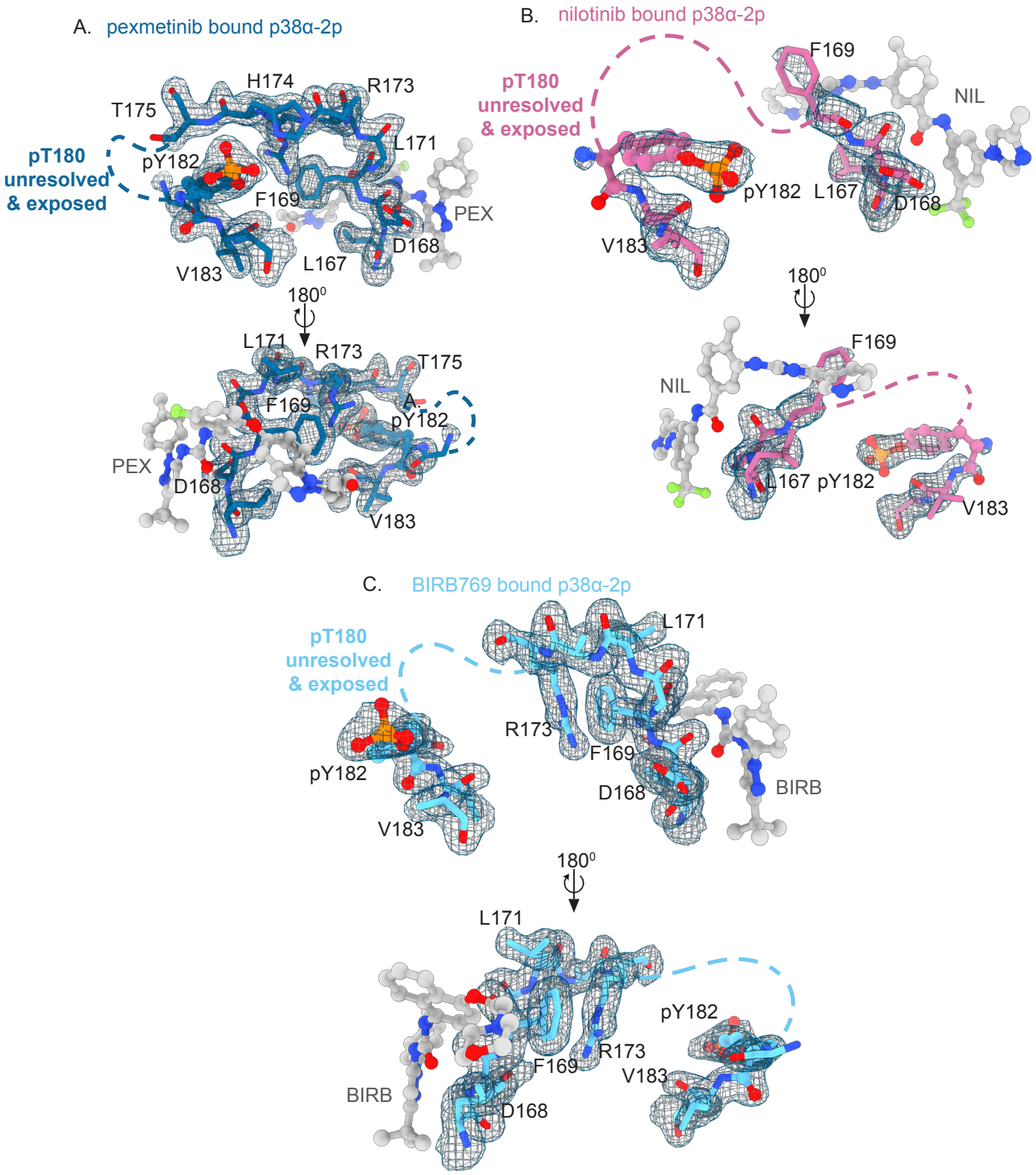

Figure S4: Activation loop of ligand bound p38α structures are differently resolved. (A) 2Fo-Fc electron density (contoured at 1 σ within 1.5 Å) of activation-loop (167-184) in p38α-2p bound to pexmetinib model. Residues are shown as sticks and pY182 is shown as spheres and sticks. Bottom panel is a 180° rotation of top panel as indicated by the arrow. (B) 2Fo-Fc electron density (contoured at 1 σ within 1.5 Å) of activation loop (167-184) in p38α-2p bound to nilotinib model. Residues are shown as sticks and pY182 is shown as spheres and sticks. Bottom panel is a 180° rotation of top panel as indicated by the arrow. (C) 2Fo-Fc electron density (contoured at 1 σ within 1.5 Å) of activation loop (167-184) in p38α-2p bound to BIRB796 model. Residues are shown as sticks and pY182 is shown as spheres and sticks. Bottom panel is a 180° rotation of top panel as indicated by the arrow. In all structures, oxygen, nitrogen, phosphorous and fluorine atoms are colored red, blue, orange and light green, respectively.

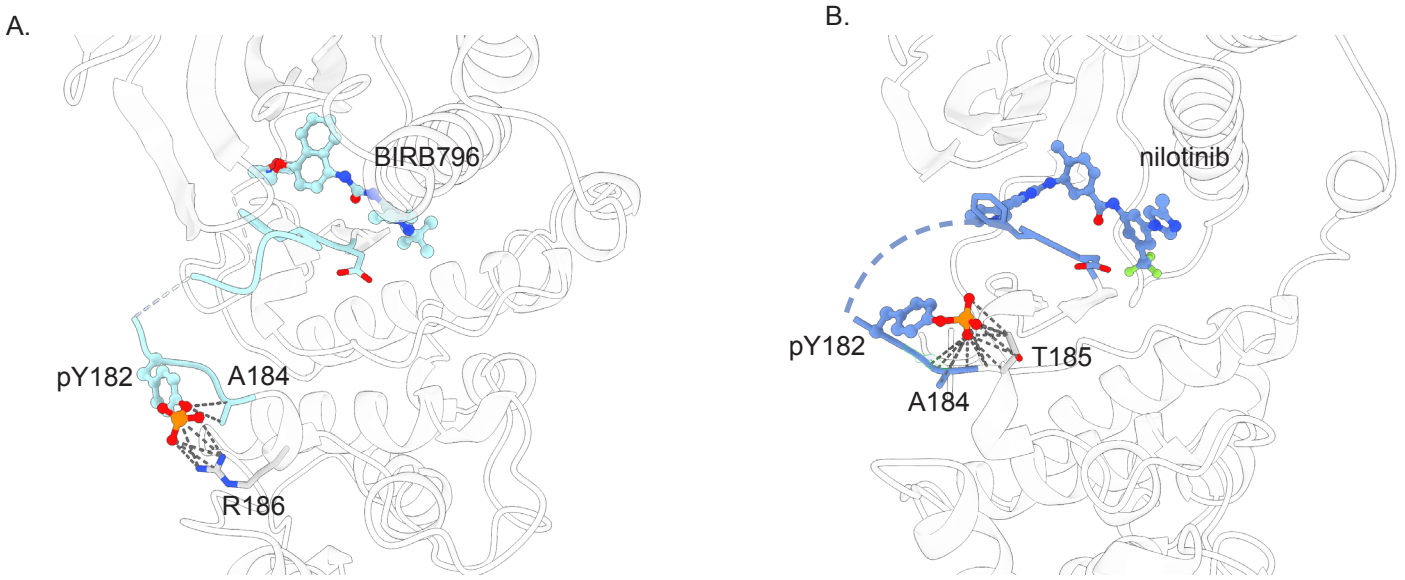

Figure S5: pY182 coordination of BIRB796 and nilotinib bound p38α-2p (A) Phosphate coordination of pY182 in p38α-2p bound to BIRB796. A184 and R186 are shown as sticks whereas pY182 is shows as spheres and sticks. (B) Phosphate coordination of pY182 in p38α-2p bound to nilotinib. A184 and T185 are shown as sticks whereas pY182 is shows as spheres and sticks In all structures, oxygen, nitrogen, phosphorous and fluorine atoms are colored red, blue, orange and light green, respectively.

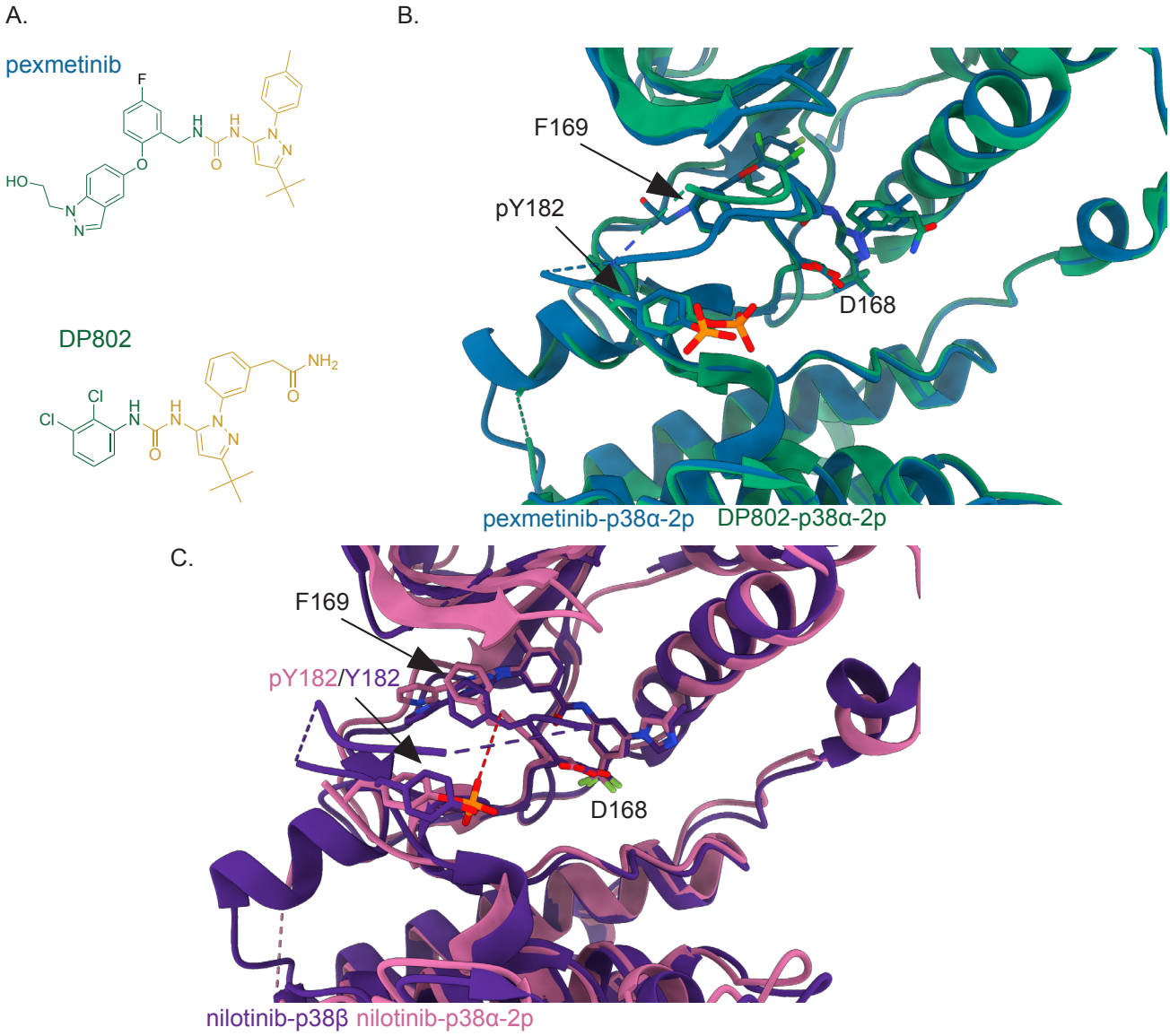

Figure S6: p38α activation-loop flip is observed in existing structures. (A) Chemical structure of pexmetinib (top) and DP802 (bottom) colored with the ATP binding pocket motif in green and the allosteric binding site motif in yellow. (B) Overlay of X-ray crystal structures of p38α-2p bound pexmetinib (blue) with p38α-2p bound to DP802 (green; PDB:3NNX). D168, F169, and pY182 are shown as sticks. (C) Overlay of X-ray crystal structures of p38α-2p bound nilotinib (pink) with p38β bound nilotinib (purple; PDB:3GP0). D168, F169, Y182 (purple) and pY182 (pink) are shown as sticks. In all structures oxygen, nitrogen, phosphorous and fluorine atoms are colored red, blue, orange and light green, respectively.

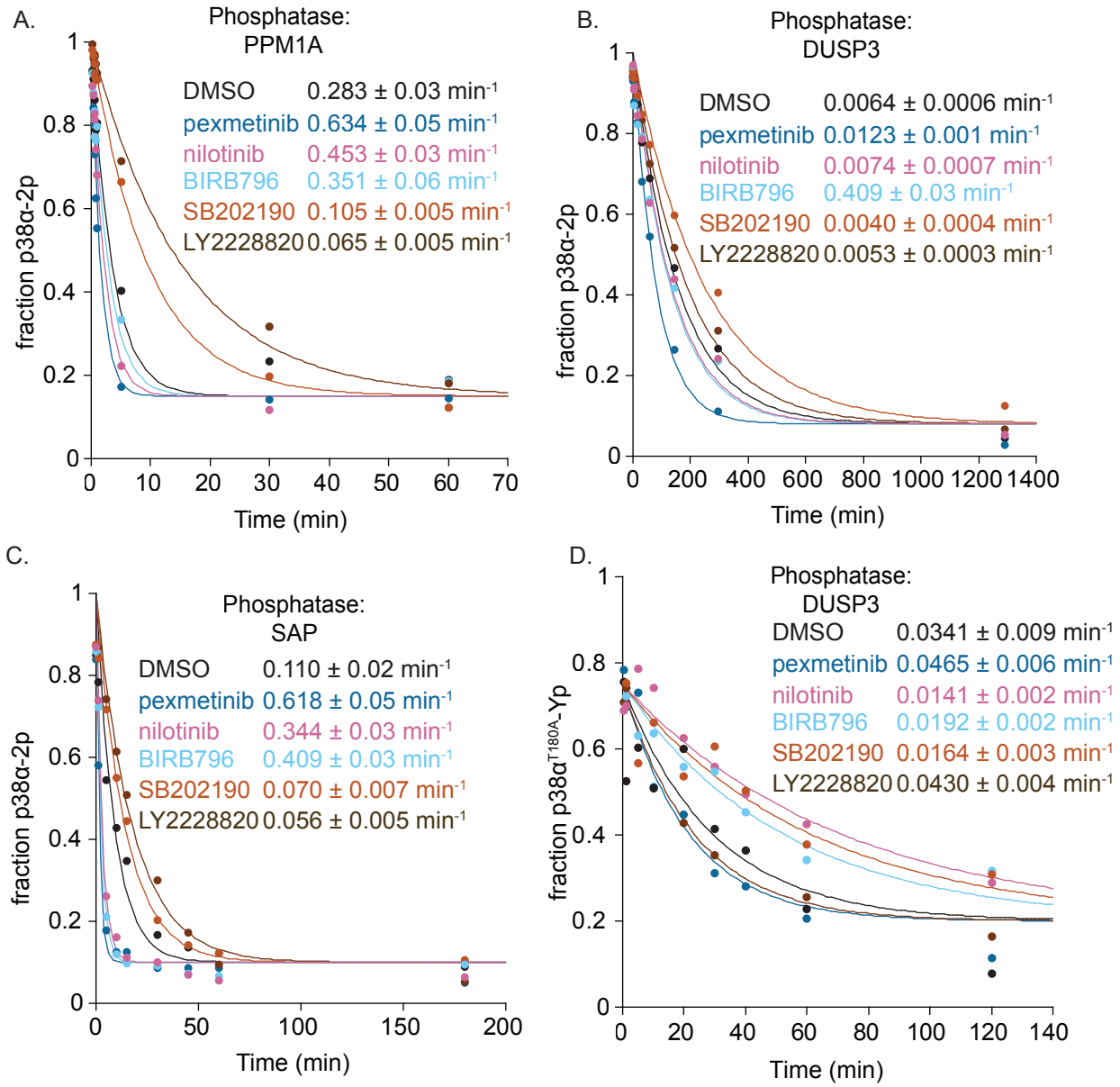

Figure S7: p38α dephosphorylation rates differ between phosphatases. (A-C) Single turnover kinetics of p38α-2p (0.25 μM) dephosphorylation by (A) PPM1A (0.5 μ M), (B) DUSP3 (50 μM), and (C) SAP (1 μM) in the absence or presence of excess inhibitor (1.25 μM). (A) PPM1A was measured at room temperature while (B) DUSP3 and (C) SAP were measured at 37 °C to increase rate of dephosphorylation. All data is fit to an exponential decay (n=2 ± error of the fit). (D) Single turnover kinetics of p38α^{T180A}-p (0.25 μM) dephosphorylation by DUSP3 (15 μM) in the absence or presence of excess inhibitor (1.25 μM) conducted at room temperature. All data is fit to an exponential decay (n=2 ± error of the fit). Data corresponds to fig 4A-B respectively.

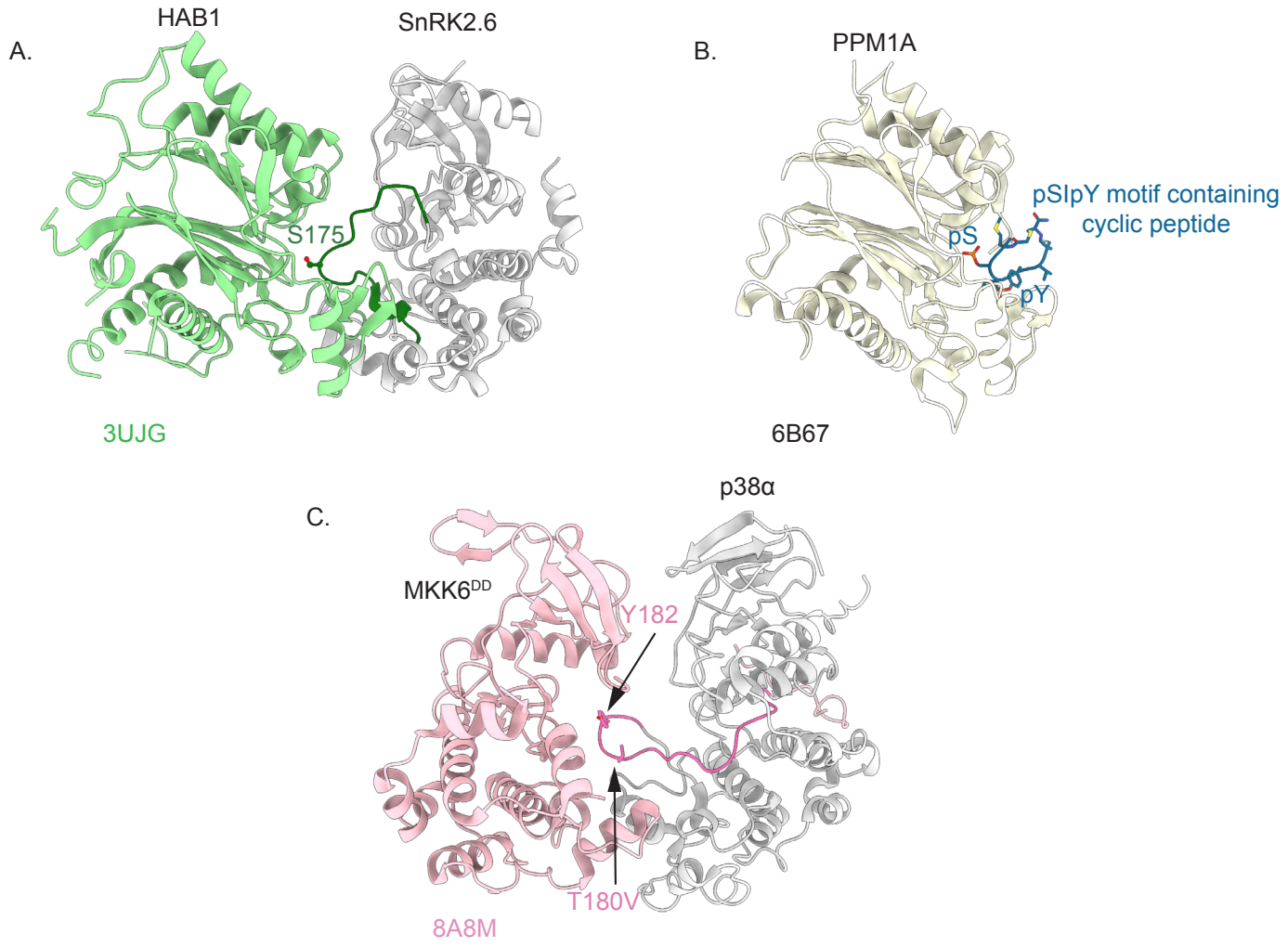

Figure S8: Activation-loop shift is required for phosphorylation and dephosphorylation of the activation-loop phospho-sites in kinases. (A) PPM plant phosphatase HAB1 (light green) bound to unphosphorylated SnRK2.6 kinase (white; A-loop in dark green) (PDB:3UJG). (B) Human phosphatase PPM1A (yellow) bound to a pSIpY motif containing cyclic peptide (blue) (PDB:6B67) (C) Ser/Thr kinase MKK6DD(pink) bound to unphosphorylated p38αT180V(white; A-loop in pink) (PDB:8A8M). In all structures, oxygen, nitrogen, phosphorous and fluorine atoms are colored red, blue, orange and light green, respectively.